Chinese Chemical Letters 35 (2024) 108736

Contents lists available at ScienceDirect

Chinese Chemical Letters

journal homepage: www.elsevier.com/locate/cclet

Polyoxometalate-organic cage with $\{Ni_4SiW_9\}$ node for photocatalytic hydrogen evolution

Jing Li, Yeqin Feng, Fangyu Fu, Xing Xin, Guoyu Yang*, Hongjin Lv*

MOE Key Laboratory of Cluster Science, Beijing Key Laboratory of Photoelectroic/Electrophotonic Conversion Materials, School of Chemistry and Chemical Engineering, Beijing Institute of Technology, Beijing 102488, China

ARTICLE INFO

Article history:
Received 26 April 2023
Revised 25 June 2023
Accepted 26 June 2023
Available online 28 June 2023

Keywords:
Polyoxometalate
Polyoxometalate-organic cages
Photocatalytic hydrogen production
Visible light illumination

ABSTRACT

The design and syntheses of metal-organic cages (MOCs) based on polyoxometalates (POMs) building blocks have attracted increasing attention due to their intriguing molecular architectures and physicochemical properties. In this work, we have successfully synthesized and systematically characterized a tetrahedral polyoxometalate-based organic cage (POC), $K_3Na_{17}H_{12}[(C_4H_6O_6)_6[Ni_4(OH)_3(A\text{-}\alpha\text{-}SiW_9O_{34})]_4]\cdot 96H_2O$ ($Ni_{16}L_6(SiW_9)_4$), using tritopic Ni_4-substituted Keggin cluster (Ni_4SiW_9) as nodes and flexible L-(+)-tartaric acid ligands as linkers. The resulting POC tetrahedron has been firstly investigated as efficient catalyst for visible-light-driven hydrogen production, achieving a turnover number of 15,500 after 96-h photocatalysis. Such high catalytic performance of $Ni_{16}L_6(SiW_9)_4$ POC catalyst could be attributed to its unique cage structure, thereby offering more efficient catalytic component accessibility. In addition, spectroscopic analyses illustrated the photocatalytic mechanism and the structural stability of the TBA-$Ni_{16}L_6(SiW_9)_4$ catalyst during the photocatalytic process.

Metal-organic cages (MOCs) are usually assembled from metal nodes (ions or clusters) and polydentate organic linkers, which are also known as metal-organic polyhedra or metal-organic supercontainers [1–3]. Although the composition and assembling principle of MOCs is similar to that of metal-organic framework (MOFs) [4–6], MOCs exhibit different characteristics from MOFs in terms of structure, dimension, molecular weight, solubility, and stability, *etc*. [7–9]. Polyhedral MOCs can be categorized as several subclasses, including tetrahedron, octahedron, cube, dodecahedron, icosahedron, cuboctahedron, truncated regular polyhedral, and prisms [10–16]. The properties of MOCs are highly dependent on their compositional metals, organic ligands, and molecular structures. Thus, delicate control of these factors could intentionally develop MOCs materials with intriguing functions and applications in molecular devices [17], catalysis [18,19], host-guest chemistry [20,21], gas/solution separation and storage [22–25], and photo-/electro-catalysis reaction [26].

Polyoxometalates (POMs), a unique class of nanoscale metal oxygen–anion clusters, are formed through the condensation of early transition metalates in their high oxidation states (Mo, W, V, Nb, Ta, *etc*.) [27–31]. POMs are desirable inorganic building blocks owing to their rich redox chemistry, tunable electronic structure, and thermally and oxidatively stability [32,33]. The design and synthesis of POM-organic cages (POCs) combined the advantages of their constituent POMs and organic linkers to generate nanocages with unprecedented properties are highly desired. To date, most POCs were constructed by polyoxovanadates and polyoxotungstates as secondary building units (SBUs) [12,34–38]. The construction of POCs using transition-metal-substituted POMs as building nodes have been far more less explored. Some representative examples include: Yang and co-workers reported the first polyoxotungstates Ni_6-substituted $\{PW_9\}$ cluster-based POC, which linked by rigid 1,3,5-benzenetricarboxylate ligand under hydrothermal conditions [11] (Scheme 1, $Ni_6SiW_9 + L_7$). Then, Fang and co-workers have constructed a family of discrete POCs with the general formula $POM_{2n}L_{3n}$ using Ni_4SiW_9 as nodes and rigid dicarboxylate as linkers (Scheme 1, $Ni_4SiW_9 + L_1/L_2/L_3/L_5/L_6$) [39], in which the photocatalytic CO_2 reduction activities of these POCs have been investigated. More recently, Zhan group reported the self-assembly of anionic POC architecture $\{Ni_6L_3SiW_9\}_4$ comprising hexanuclear nickel-substituted POM clusters and p-aminobenzoic acid ligands (Scheme 1, $Ni_6SiW_9 + L_4$) [40].

In addition to the structural diversity of POMs, transition-metal-substituted POMs have been energetically investigated as catalysts for light-driven hydrogen evolution [41–51]. In this scenario, we expected that the POCs constructed by transition-metal-substituted POMs nodes and organic ligands might exhibit a synergistic

* Corresponding authors.
E-mail addresses: ygy@bit.edu.cn (G. Yang), hlv@bit.edu.cn (H. Lv).

https://doi.org/10.1016/j.cclet.2023.108736
1001-8417/

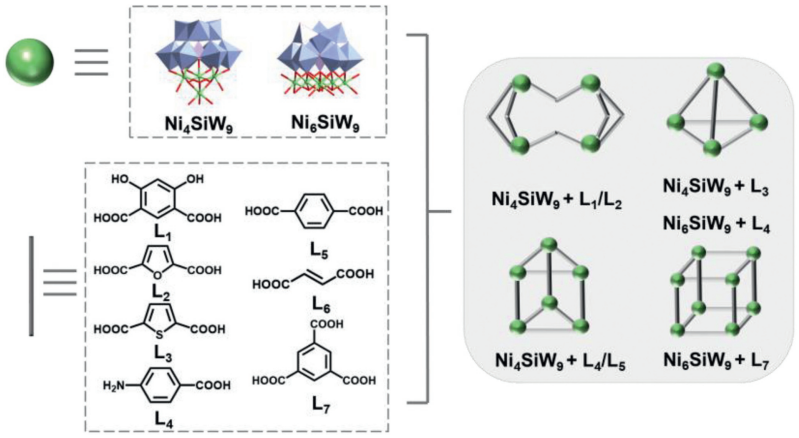

Scheme 1. Three-connected $\{Ni_4SiW_9\}$ and $\{Ni_6PW_9\}$ SBUs (green nodes) and rigid dicarboxylate linkers (including seven ligands) combine to form some POCs components (schematic representation).

cooperation between the constituent POMs and distinct cage structures for better catalytic performance. Moreover, their unique cage architecture may work as perfect nanoreactor with efficient accessibility to catalytic components.

In this context, we report herein the successful construction of a tetrahedral POC, $K_3Na_{17}H_{12}[(C_4H_6O_6)_6[Ni_4(OH)_3(A\text{-}\alpha\text{-}SiW_9O_{34})]_4]\cdot 96H_2O$ ($Ni_{16}L_6(SiW_9)_4$), using Ni_4SiW_9 as the SBUs and L-(+)-tartaric acid (L) as linkers. The resulting POC tetrahedron has been firstly investigated as efficient catalyst for visible-light-driven hydrogen production when coupling with $[Ir(coumarin)_2(dtbbpy)][PF_6]$ (PS) as the photosensitizer, TEOA as the sacrificial electron donor, and H_2O as the proton source.

Single crystal X-ray analyses reveal that $Ni_{16}L_6(SiW_9)_4$ crystallizes in the cubic space group *I23* (Table S1 in Supporting information) and exhibits a POM-organic tetrahedral cage constructed by four Ni_4SiW_9 SBUs and six L linkers (Fig. 1a). The four Ni-substituted Ni_4SiW_9 SBUs are located at the vertex of the tetrahedron, while the L ligands are disposed on the six edges to form an interior cavity with a void space of about 102 $Å^3$ as illustrated by a simulated yellow ball (Fig. 1a, see calculation method in Supporting information). The angles between nearby L ligands are measured as ~76° from each other, which is close to the value of the acetate-chelated derivative as reported by Mialane *et al.* [52]. From a different point of view, the polyoxoanion $Ni_{16}L_6(SiW_9)_4$ can be structurally regarded as a central $\{Ni_4(HO)_3\}_4(C_4H_6O_6)_6\}$ moiety capped by four lacunary A-α-$\{SiW_9O_{34}\}$ ligands (Fig. 1b). In the

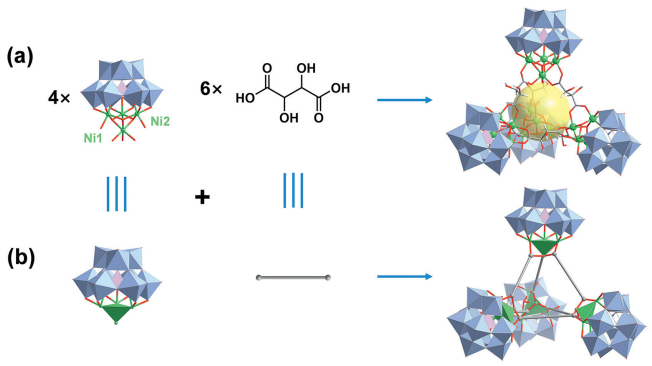

Fig. 1. (a) Combined polyhedral/ball-and-stick representations of the polyoxoanion $Ni_{16}L_6(SiW_9)_4$, the polyhedral structure of Ni_4SiW_9 and tartaric acid linker (L), (b) simplified model representations of the Ni_4SiW_9 building blocks, ball-and-stick model of L, and polyoxoanion $Ni_{16}L_6SiW_9$. Color code: WO_6 (light purple octahedra), L (gray stick), SiO_4 (pick tetrahedra), Ni (green balls), H (white balls), O (red balls).

C_{3v}-symmetric Ni_4SiW_9 SBU, three crystallographically-equivalent Ni^{II} ions (denoted as Ni2) in the pseudo cubane-type $\{Ni_4O_3\}$ cluster are stabilized in the trivacant sites of A-α-$\{SiW_9O_{34}\}$ ligand, while another one Ni^{II} ion (denoted as Ni1) caps on three Ni2 atoms *via* three acetate bridges and three OH ligands with a C_3 axis passing through Ni1 and the Si heteroatom (Fig. 1a). Each Ni_4SiW_9 SBU is coordinated by three organic ligands, all hydroxyl groups of L-(+)-tartaric acid ligands in the molecular structure point into the exterior cavity (Fig. 1a). The bond lengths of Ni–O bonds in Ni_4SiW_9 range from 2.002 to 2.065 Å. Bond valence sum (BVS) calculations (Table S2 in Supporting information) and charge balance requirements confirm that the +2 oxidation states of Ni1 and Ni2, and the valence of W and Si are +6 and +4, respectively. BVS values of the μ_3-O atoms (pink balls in Fig. S1 in Supporting information) are calculated as about 1.14, indicating the monoprotonation of these μ_3-O atoms (Table S2). It is worth mentioning that the synthesis of Ni_4SiW_9-based POC using the organic succinic acid ligand was unsuccessful, which could be attributed to the increased rigidity of the organic chain due to the presence of hydroxyl groups in L ligand. Recently, the structurally-similar tetrahedral POC has also been reported Fang and co-workers [39], $Na_{30}Ni[\{(A\text{-}\alpha\text{-}SiW_9O_{34})Ni_4(OH)_3\}_4(OOC(C_4H_2S)COO)_6]\cdot 72H_2O$, in which four Ni_4SiW_9 SBUs were also used as the nodes of POC, instead six more rigid dicarboxylate ligands (2,5-thiophenedicarboxylate) were used as linkers (Scheme 1, Ni_4SiW_9 + L_3).

The molecular structure of $Ni_{16}L_6(SiW_9)_4$ was characterized by FT-IR spectrum. The characteristic bands in the range of 1200–400 cm^{-1} can be assigned to the Si–O, W–O, and W–O–W vibrational bands (Fig. S2 in Supporting information). The IR bands in the range of 1200–400 cm^{-1} also show the characteristic vibrations of L ligands as expected. In addition, the FT-IR spectra before and after counter cations exchange from Na^+/K^+ to TBA^+ showed all the characteristic bands of polyoxoanion $Ni_{16}L_6(SiW_9)_4$, confirming the retained molecular skeleton of $Ni_{16}L_6(SiW_9)_4$. Also, thermogravimetric analysis showed a 22% weight loss percentage, corresponding to a total of 96 crystallization water molecules per formula unit (Fig. S3 in Supporting information). The elemental composition of $Ni_{16}L_6(SiW_9)_4$ complex was also characterized by scanning electron microscopy and energy dispersive X-ray spectroscopy (SEM/EDS), revealing the microscopic morphology of the $Ni_{16}L_6(SiW_9)_4$ crystals and the presence of Ni, W, and Si elements (Fig. S4 in Supporting information). X-ray photoelectron spectroscopy (XPS) has also been utilized to assess the presence of Si, Ni, and W elements (Fig. 2a) as well as their corresponding chemical oxidation states (Figs. 2b-d). The binding energies at 855.8 and 873.7 eV were assigned to the signals of Ni $2p_{3/2}$ and Ni $2p_{1/2}$, respectively (cor-

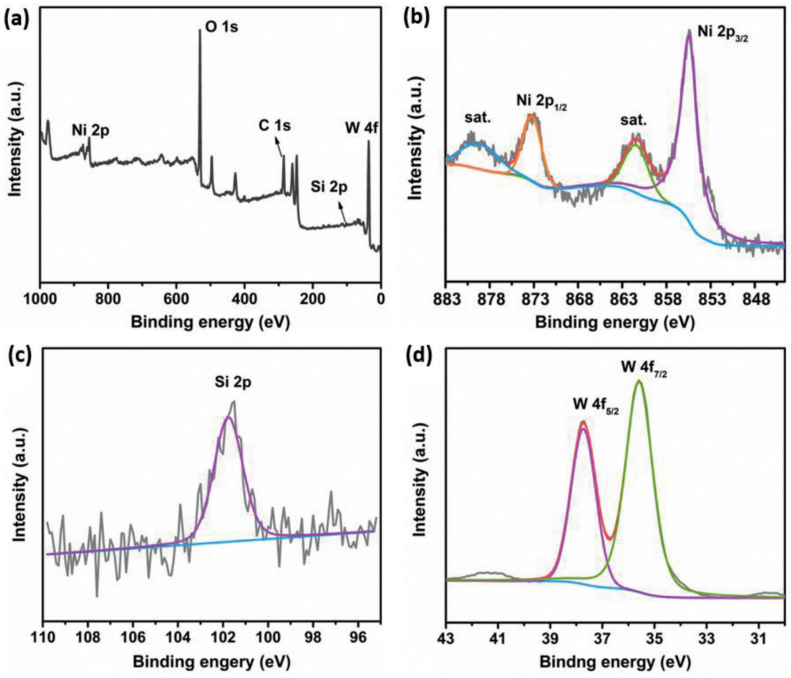

Fig. 2. (a) X-ray photoelectron spectroscopy survey spectra of $Ni_{16}L_6(SiW_9)_4$ and high-resolution X-ray photoelectron spectroscopy spectra of (b) Ni 2p, (c) Si 2p, and (d) W 4f signals in $Ni_{16}L_6(SiW_9)_4$.

responding satellite peaks at 861.9 and 879.9 eV), indicating the oxidation state of Ni is +2. While the W 4f XPS signal can be deconvoluted into W $4f_{5/2}$ and $4f_{7/2}$ at binding energies of 37.5 and 35.8 eV, respectively, indicating a +6 oxidation state. The Si 2p signal exhibits a binding energy of 101.8 eV, corresponding to a +4 oxidation state.

The TBA salt of polyoxoanion $Ni_{16}L_6(SiW_9)_4$ (TBA-$Ni_{16}L_6(SiW_9)_4$) was subsequently employed as the molecular catalyst for visible-light-driven hydrogen evolution in a well-established three-component catalytic system using $[Ir(coumarin)_2(dtbbpy)]^+$ [53] as the photosensitizer, TEOA as the sacrificial electron donor, and H_2O as the proton source. The photocatalysis was performed in a CH_3CN/DMF (v/v = 1/3) solution under a Xe-lamp light source equipped with a 400 nm cut off filter at 20 °C. As shown in Figs. 3a-c, varying the concentration of each essential component can also greatly adjust the efficiency of H_2 production. For instance, increasing the concentration of TBA-$Ni_{16}L_6(SiW_9)_4$ from 0 μmol/L to 25 μmol/L leads to the enhancement of H_2 yield from ~1.98 μmol to ~321.47 μmol in 5 h (Fig. 3a), corresponding to the TONs of 4619 (5 μmol/L catalyst), 3618 (10 μmol/L catalyst), 3403 (15 μmol/L catalyst), 2677 (20 μmol/L catalyst), and 2143 (25 μmol/L catalyst), respectively (Fig. S5a in Supporting information). The optimized TON (~4619) is calculated at a TBA-$Ni_{16}L_6(SiW_9)_4$ concentration of 5 μmol/L, because a given catalyst at relatively low concentration may possibly work as the limiting parameter for reaching a higher TON [54]. Specifically, during photocatalytic reaction, the photosensitizer is excited to generate photogenerated electrons and holes, which are harvested by TEOA and the catalyst, respectively. When the catalyst concentration is very low, the effective numbers of electrons received by per catalyst become the rate-limiting factor for catalysis, thereby leading to a higher TON value. In other control experiment, turning the concentration of $[Ir(coumarin)_2(dtbbpy)]^+$ photosensitizer (PS) from 0 to 0.3 mmol/L increased the H_2 yield 64.13 μmol to 162.96 μmol (Fig. 3b). It is also noted that the increment of TEOA concentration from 0.35 mol/L to 0.50 mol/L does not greatly enhance the H_2 production (Fig. 3c), indicating that the concentration of TEOA higher than 0.35 mol/L is no longer the rete-limiting factor for photocatalysis. After 5-h photocatalysis, a TON of as high as 6834 has been achieved, which represents one of the highest values in terms of known Ni-substituted POM-catalyzed H_2 production systems (Table S3 in Supporting information). Therefore, an optimal TEOA concentration of 0.35 mol/L is used for further study. To better understand the catalytic system, several control experiments were conducted to assess the importance of each component for photocatalytic hydrogen generation. As shown in Fig. 3d, the absence of any components (catalyst, sacrificial reagent, or photosensitizer) resulted in negligible hydrogen production, and the optimal photocatalytic system exhibited the highest TON value among various control experiments (Fig. S5b in Supporting information). The catalytic system only produced very little amount of H_2 gas while replacing the TBA-$Ni_{16}L_6(SiW_9)_4$ catalyst with TBA-SiW_9, revealing the significance of the Ni active sites. In addition, the replacement of TBA-$Ni_{16}L_6(SiW_9)_4$ catalyst with molar equivalents of $Ni(NO_3)_2{\cdot}4H_2O$, TBA-SiW_9, and L ligands also led to inefficient H_2 production. These results confirm that the catalyst, photosensitizer, and sacrificial reagent are all indispensable factors, and the special molecular skeleton of TBA-$Ni_{16}L_6(SiW_9)_4$ is extremely crucial for efficient photocatalysis.

To prove the important molecular cage structure of TBA-$Ni_{16}L_6(SiW_9)_4$ catalyst, we have compared its catalytic performance with that of our previously-reported Ni_{16}-containg POM catalyst [42], TBA-$Ni_{16}(PO_4)_4(PW_9)_4$, which is also characterized by FT-IR spectra (Fig. S6 in Supporting information). Under otherwise identical conditions, the hydrogen production of TBA-$Ni_{16}L_6(SiW_9)_4$ is much higher than that of TBA-$Ni_{16}(PO_4)_4(PW_9)_4$ (Fig. S7 in Supporting information). Such distinct catalytic performance could be attributed to the unique cage structure of the $Ni_{16}L_6(SiW_9)_4$ POCs, which could not only provide good transportation of catalytic components *via* a possible substrate channeling effect, but also offer more accessible catalytic active sites for H_2 production.

Then, the stability of catalyst and robustness of the catalytic system have been further investigated by various experiments.

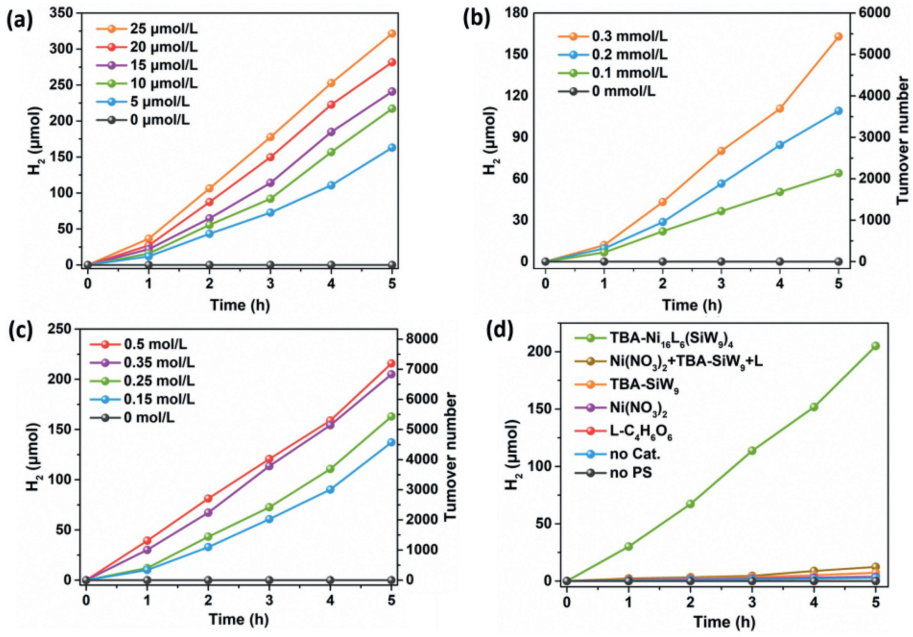

Fig. 3. Photocatalytic H_2 production at different concentrations of (a) TBA-$Ni_{16}L_6(SiW_9)_4$ catalyst (0–25 μmol/L) at 0.25 mmol/L PS, 0.25 mol/L TEOA, (b) PS (0–0.3 mmol/L) at 0.25 mol/L TEOA, 5 μmol/L catalyst, and (c) TEOA (0–0.5 mol/L) at 0.3 mmol/L PS, 5 μmol/L catalyst. (d) Control experiments of photocatalytic H_2 production at different conditions. Standard conditions: 300 W Xe lamp (400 nm cutoff filter), PS (0.3 mmol/L), catalyst (5 μmol/L), TEOA (0.35 mol/L), H_2O (1.4 mol/L), and CH_3CN/DMF (v/v = 1:3) deaerated with Ar/CH_4 (v/v = 4:1).

Firstly, a Hg-poisoning test by adding 20 mg Hg to the photocatalytic system does not significantly decrease the hydrogen evolution, eliminating the formation of potential metal nanoparticles from the decomposition of TBA-$Ni_{16}L_6(SiW_9)_4$ catalyst (Fig. S8 in Supporting information). Secondly, the long-term catalytic reaction up to 96 h produced ~450 μmol of H_2, corresponding to a TON of ~15,000, indicating the long-term robustness of the TBA-$Ni_{16}L_6(SiW_9)_4$ catalyst (Fig. S9 in Supporting information). The declining hydrogen production rate at prolonged reaction time could be attributed to (1) the consumption of TEOA that may change the environment of the photocatalytic reaction system, (2) the slight decomposition of $[Ir(coumarin)_2(dtbbpy)]^+$ photosensitizer that leads to the decreased utilization efficiency of incident photons. Thirdly, to better assess the stability of the catalyst, DLS measurement was also utilized to examine the homogeneity of the $Ni_{16}L_6(SiW_9)_4$-catalyzed reaction. The DLS signal centered at 1.2 nm was observed after 5-h photocatalysis (Fig. S10 in Supporting information), which is consistent with the hydrodynamic diameter of TBA-$Ni_{16}L_6(SiW_9)_4$ (5 μmol/L) before catalysis. Moreover, the structural integrity of the TBA-$Ni_{16}L_6(SiW_9)_4$ catalyst has also been characterized by their FT-IR spectra before and after photocatalysis. Basically, an excessive amount of $[Ru(bpy)_3]^{2+}$ was added to the reaction solution to separate the catalyst after photocatalysis, forming a {$[Ru(bpy)_3]$-$Ni_{16}L_6(SiW_9)_4$} precipitate. The FT-IR spectra of isolated {$[Ru(bpy)_3]$-$Ni_{16}L_6(SiW_9)_4$} precipitate before and after photocatalysis retained all characteristic bands of TBA-$Ni_{16}L_6(SiW_9)_4$ catalyst, further confirming the structural stability of the TBA-$Ni_{16}L_6(SiW_9)_4$ catalyst (Fig. S11 in Supporting information).

To reveal the photocatalytic mechanism, the emission quenching of $[Ir(coumarin)_2(dtbbpy)]^+$ by either TEOA or TBA-$Ni_{16}L_6(SiW_9)_4$ was monitored in an inert atmosphere by using steady-state and time-resolved luminescence spectroscopy. The addition of either 5 μmol/L TBA-$Ni_{16}L_6(SiW_9)_4$ catalyst or 0.35 mol/L TEOA electron donor can cause the emission quenching of $[Ir(coumarin)_2(dtbbpy)]^{+*}$ (Fig. 4a). The single-exponential decay kinetics of excited-state $[Ir(coumarin)_2(dtbbpy)]^{+*}$ luminescence in the presence of TEOA and TBA-$Ni_{16}L_6(SiW_9)_4$ exhibited a decreased lifetimes from 1131.6 ns to 887.8 ns and 927.8 ns (Fig. 4b), respectively. These results proved the presence of both oxidative and reductive quenching processes during photocatalysis. The emission intensity of $[Ir(coumarin)_2(dtbbpy)]^{+*}$ was gradually quenched with the addition of TBA-$Ni_{16}L_6(SiW_9)_4$ (from 0 to 60 μmol/L) or TEOA (from 0 to 0.35 mol/L) (Figs. 4c and d). The linear Stern-Volmer plots give rise to an oxidative quenching rate constant (k_{oq}) by TBA-$Ni_{16}L_6(SiW_9)_4$ of 4.1×10^9 L mol^{-1} s^{-1} (Fig. S12 in Supporting information) and a reductive quenching rate constant (k_{rq}) by TEOA of 2.2×10^6 L mol^{-1} s^{-1} (Fig. S13 in Supporting information). Even though the koq value is three times orders of magnitude higher than the k_{rq} value due to the strong electrostatic interaction between the cationic $[Ir(coumarin)_2(dtbbpy)]^+$ and the anionic $Ni_{16}L_6(SiW_9)_4$ catalyst, the reduction quenching pathway is still regarded as a dominant one due to the much higher concentration of TEOA (0.35 mol/L) than that of TBA-$Ni_{16}L_6(SiW_9)_4$ (5 μmol/L), corresponding to a calculated quenching rate of 7.8×10^5 s^{-1} and 2.1×10^4 s^{-1}, respectively.

In summary, an unprecedented tetrahedral POC architecture $K_3Na_{17}H_{12}[(C_4H_6O_6)_6[Ni_4(OH)_3(A\text{-}\alpha\text{-}SiW_9O_{34})]_4]\cdot 96H_2O$ has been successfully synthesized using flexible L ligand and Ni_4SiW_9 POM SBUs. Such $Ni_{16}L_6(SiW_9)_4$ tetrahedron was constructed by four Ni_4SiW_9 SBUs and six L linkers to form a cage structure with a void space of about 102 $Å^3$. Under minimally optimized conditions, the TBA-$Ni_{16}L_6(SiW_9)_4$-catalyzed hydrogen production system produces a TON of 6834 after 5-h reaction, and the TON value steadily increases to an extraordinary level of approximately 15,500 while prolonging the reaction time to 96-h. Spectroscopic analyses confirmed that the photocatalytic mechanism includes both the reductive and oxidative quenching pathways. In addition, a series of experimental evidence (*e.g.*, Hg-poisoning test, DLS measurements and FT-IR spectra of the isolated catalyst before and after photocatalysis) confirmed the structural stability of the TBA-$Ni_{16}L_6(SiW_9)_4$ catalyst during the photocatalytic process. Due to the unique cage structure of the $Ni_{16}L_6(SiW_9)_4$ POCs, more effi-

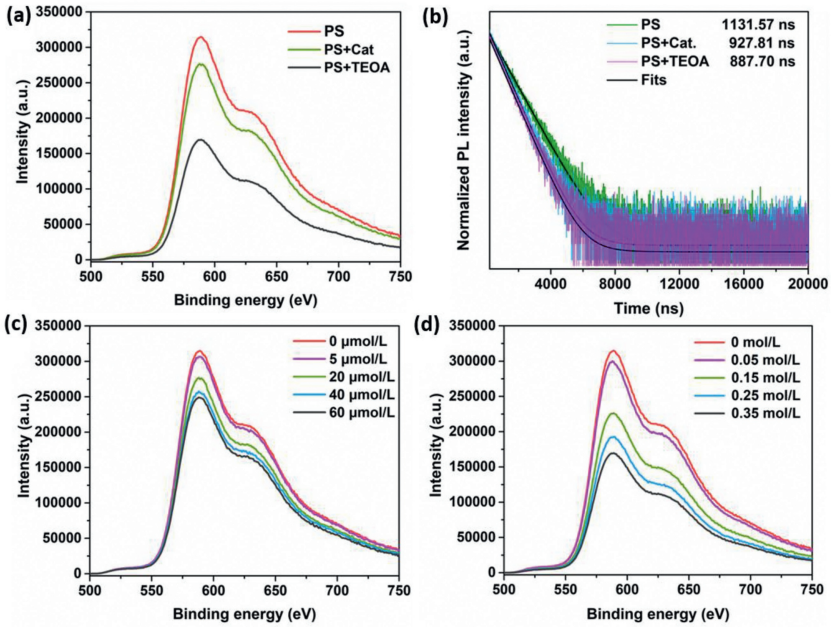

Fig. 4. (a) Emission spectra (λ_{ex} = 460 nm) of photosensitizer (0.3 mmol/L) (red), with added 5 μmol/L TBA-$Ni_{16}L_6(SiW_9)_4$ (green) or 0.35 mol/L TEOA (dark blue). (b) Normalized time-resolved luminescence decay kinetics (λ_{em} = 589 nm) of PS, PS with TBA-$Ni_{16}L_6(SiW_9)_4$ (blue), and PS with TEOA (purple). Emission quenching of excited state PS (0.3 mmol/L) by different concentrations of (c) TBA-$Ni_{16}L_6(SiW_9)_4$ (0–60 μmol/L) and (d) TEOA (0–0.35 mol/L) in 3 mL of CH_3CN/DMF (v/v = 1/3) solution under Ar condition upon 450 nm excitation. Conditions: PS (0.3 mmol/L), TEOA (0.35 mol/L), and catalyst TBA-$Ni_{16}L_6(SiW_9)_4$ (5 μmol/L).

cient catalytic component accessibility would be expected in the case of TBA-$Ni_{16}L_6(SiW_9)_4$-catalyzed reaction system compared to that of the cage-free TBA-$Ni_{16}(PO_4)_4(PW_9)_4$-catalyzed system. This work not only enriches the family of POM-based organic cages, but also extends new catalytic applications of POCs in solar-driven hydrogen production.

Declaration of competing interest

The authors declare that they have no known competing financial interests or personal relationships that could have appeared to influence the work reported in this paper.

Acknowledgments

This work was financially supported by the National Natural Science Foundation of China (Nos. 21871025 and 21831001), the Recruitment Program of Global Experts (Young Talents) and BIT Excellent Young Scholars Research Fund. The instrumental support from the Analysis and Testing Center of Beijing Institute of Technology is also highly appreciated.

Supplementary materials

Supplementary material associated with this article can be found, in the online version, at doi:10.1016/j.cclet.2023.108736.

References

[1] S. Lee, H. Jeong, D. Nam, et al., Chem. Soc. Rev. 50 (2021) 528–555.
[2] D.J. Tranchemontagne, Z. Ni, M. O'Keeffe, et al., Angew. Chem. Int. Ed. 47 (2008) 5136–5147.
[3] Z. Gao, J. Jia, W. Fan, et al., Chin. Chem. Lett. 33 (2022) 4415–4420.
[4] S. Guo, L.H. Kong, P. Wang, et al., Angew. Chem. Int. Ed. 61 (2022) e202206193.
[5] T.C. Zhuo, Y. Song, G.L. Zhuang, et al., J. Am. Chem. Soc. 143 (2021) 6114–6122.
[6] Z. Wu, S. Guo, L.H. Kong, et al., Chin. J. Catal. 42 (2021) 1790–1797.
[7] B.S. Pilgrim, N.R. Champness, ChemPlusChem 85 (2020) 1842–1856.
[8] J. Liu, Z. Wang, P. Cheng, et al., Nat. Rev. Chem. 6 (2022) 339–356.
[9] S.P. Zheng, Y.W. Xu, P.Y. Su, et al., Chin. Chem. Lett. 34 (2023) 108477.
[10] B. Hou, X. Gu, H. Gan, et al., Inorg. Chem. 61 (2022) 7103–7110.
[11] S.T. Zheng, J. Zhang, X.X. Li, et al., J. Am. Chem. Soc. 132 (2010) 15102–15103.
[12] Y. Zhang, H. Gan, C. Qin, et al., J. Am. Chem. Soc. 140 (2018) 17365–17368.
[13] H. Gan, N. Xu, C. Qin, et al., Nat. Commun. 11 (2020) 4103.
[14] S. Furukawa, N. Horike, M. Kondo, et al., Inorg. Chem. 55 (2016) 10843–10846.
[15] S.P. Argent, H. Adams, et al., J. Am. Chem. Soc. 128 (2006) 72–73.
[16] S. Wang, X. Gao, X. Hang, et al., J. Am. Chem. Soc. 138 (2016) 16236–16239.
[17] X.Y. Zheng, X.J. Kong, Z. Zheng, et al., Acc. Chem. Res. 51 (2018) 517–525.
[18] Y. Xue, X. Hang, J. Ding, et al., Coord. Chem. Rev. 430 (2021) 213656.
[19] C.M. Hong, R.G. Bergman, K.N. Raymond, et al., Acc. Chem. Res. 51 (2018) 2447–2455.
[20] S. Zarra, D.M. Wood, D.A. Roberts, et al., Chem. Soc. Rev. 44 (2015) 419–432.
[21] F.J. Rizzuto, L.K.S. von Krbek, J.R. Nitschke, Nat. Rev. Chem. 3 (2019) 204–222.
[22] L.J. Wang, S. Bai, Y.F. Han, J. Am. Chem. Soc. 144 (2022) 16191–16198.
[23] D.F. Sava, V.C. Kravtsov, J. Eckert, et al., J. Am. Chem. Soc. 131 (2009) 10394–10396.
[24] D. Zhang, T.K. Ronson, J.R. Nitschke, Acc. Chem. Res. 51 (2018) 2423–2436.
[25] L. Zhang, H. Liu, G. Yuan, et al., Chin. J. Chem. 39 (2021) 2273–2286.
[26] X.X. Li, D. Zhao, S.T. Zheng, Coord. Chem. Rev. 397 (2019) 220–240.
[27] C.L. Hill, C.M. Prosser-McCartha, Coord. Chem. Rev. 143 (1995) 407–455.
[28] L. Qiao, M. Song, A. Geng, et al., Chin. Chem. Lett. 30 (2019) 1273–1276.
[29] Y. Zhang, X.B. Han, Z.M. Zhang, et al., Chin. Chem. Lett. 24 (2013) 581–584.
[30] X.Y. Zhou, F. Wang, J. Zhang, J. Solid State Chem. 317 (2023) 123647.
[31] Z.Y. Liu, Y.D. Lin, Y. Hao, et al., Tungsten 4 (2022) 81–98.
[32] D. Zang, H. Wang, Polyoxometalates 1 (2022) 9140006.
[33] Y. Zhang, Y. Liu, D. Wang, et al., Polyoxometalates 2 (2023) 9140017.
[34] J.M. Breen, W. Schmitt, Angew. Chem. Int. Ed. 47 (2008) 6904–6908.
[35] N. Xu, H. Gan, C. Qin, et al., Angew. Chem. Int. Ed. 58 (2019) 4649–4653.
[36] Y. Gong, C. Qin, Y. Zhang, et al., Angew. Chem. Int. Ed. 59 (2020) 22034–22038.
[37] C. Li, N. Mizuno, K. Yamaguchi, et al., J. Am. Chem. Soc. 141 (2019) 7687–7692.
[38] C. Li, K. Yamaguchi, K. Suzuki, Angew. Chem. Int. Ed. 60 (2021) 6960–6964.
[39] Q. Chang, X. Meng, W. Ruan, et al., Angew. Chem. Int. Ed. 61 (2022) e202117637.
[40] M.Y. Wang, Y.Y. Yuan, Z.Q. Qi, et al., Chem. Mater. 34 (2022) 10501–10508.
[41] H. Lv, J. Song, Y.V. Geletii, et al., J. Am. Chem. Soc. 136 (2014) 9268–9271.
[42] X.B. Han, C. Qin, X.L. Wang, et al., Appl. Catal. B 211 (2017) 349–356.
[43] H. Lv, J. Song, H. Zhu, et al., J. Catal. 307 (2013) 48–54.
[44] J. Zhao, Y. Ding, J. Wei, et al., Int. J. Hydrog. Energy 39 (2014) 18908–18918.
[45] G. Paille, A. Boulmier, A. Bensaid, et al., Chem. Commun. 55 (2019) 4166–4169.
[46] Y.S. Ding, H.Y. Wang, Y. Ding, Dalton Trans. 49 (2020) 3457–3462.
[47] L. Jiao, Y. Dong, X. Xin, et al., Appl. Catal. B 291 (2021) 120091.
[48] L. Qin, C. Zhao, L.Y. Yao, et al., CCS Chem 4 (2022) 259–271.
[49] T. Cui, L. Qin, F. Fu, et al., Inorg. Chem. 60 (2021) 4124–4132.
[50] M. Chi, H. Li, X. Xin, et al., Inorg. Chem. 61 (2022) 8467–8476.
[51] Y. Feng, L. Qin, J. Zhang, et al., Chin. J. Catal. 43 (2022) 442–450.
[52] C. Pichon, P. Mialane, A. Dolbecq, et al., Inorg. Chem. 47 (2008) 11120–11128.
[53] M. Zhang, X. Xin, Y. Feng, et al., Appl. Catal. B 303 (2022) 120893.
[54] H. Lv, Y. Gao, W. Guo, et al., Inorg. Chem. 55 (2016) 6750–6758.